Two Transport Routes for Fetuin-A-based Mineral Complexes in Osteogenic Matrix Mineralization

Authors: Judith M. Schaart[1], Luco Rutten[1,2], Shaina V. To[1], Alisha A. Shah[1], Martijn Martens[1,2], Elena Macías-Sánchez[1,2,3], Willi Jahnen-Dechent[4], Nico Sommerdijk[1,2]*, Anat Akiva[1,2]*

Affiliations

[1] Department of Medical BioSciences, Radboud University Medical Center; Nijmegen, The Netherlands

[2] Electron Microscopy Center, Radboudumc Technology Center Microscopy, Radboud University Medical Center; Nijmegen, The Netherlands

[3] Department of Cell Biology and Immunology, Institute of Parasitology and Biomedicine "López-Neyra", Spanish National Research Council (CSIC), 18016 Granada (Spain)

[4] Helmholtz Institute for Biomedical Engineering, Biointerface Laboratory, RWTH Aachen University Hospital; Aachen, Germany

* Corresponding author. Email: a.akiva@radboudumc.nl; n.sommerdijk@radboudumc.nl

Abstract

Fetuin-A is an abundant serum glycoprotein that prevents ectopic calcification. It has a high binding capacity for calcium phosphate and forms calciprotein monomers (CPM) and particles (CPP) upon binding. While it is also an abundant non-collagenous protein in bone, it's role in bone matrix mineralization remains unclear. Using DLS and liquid-phase TEM, we identified a two-phase assembly process of primary CPPs, in which small and transient particles (tCPPs) are formed initially, after which larger, stable CPPs form. Using cell-free and osteoblast-based mineralization experiments, we found that CPMs and tCPPs can directly mineralize collagen fibrils, while CPPs are only a suitable mineral source after endocytosis and processing by matrix-producing osteoblasts. This indicates the existence of two potential transport routes for Fetuin-A/mineral complexes during bone matrix formation.

Main Text

Fetuin-A (FetA), also known as α_2-Heremans Schmidt Glycoprotein, is a liver-produced glycoprotein that is secreted into the blood to prevent ectopic calcification. It has a high binding capacity for calcium phosphate (CaP), creating protein/mineral complexes called calciprotein particles thereby modulating CaP supersaturation levels in the blood. (*1-3*) Upon binding CaP, calciprotein monomers (CPMs) are formed, which continue to aggregate and start forming calciprotein particles (CPPs). Two populations of CPPs have been reported: primary CPPs (CPP1) with a spherical shape and diameters of 50-100 nm carrying amorphous calcium phosphate, and the larger ellipsoidal secondary CPPs (CPP2, 100-300 nm) that form from aging primary CPP1 and contain crystalline hydroxyapatite.(*1, 4, 5*)

The different types of FetA/mineral complexes are present in the blood in variable concentrations, dependent on the individual's health status. CPMs have been suggested to be the predominant species of FetA/mineral complexes circulating in healthy adults, (*6, 7*) and are cleared via a renal pathway. (*7, 8*) CPPs are cleared via hepatic clearance in combination with phagocytosis. Increased concentrations of CPPs have been found in pathological situations, such as chronic kidney disease, in which clearance of FetA/mineral complexes from the blood flow is affected. (*9, 10*) Secondary CPPs are rare in living individuals (*5, 11*) and have been associated with pathologies, where they can induce apoptosis (*12*) and inflammatory responses. (*8*)

Although produced in the liver, FetA is the most abundant non-collagenous protein in bone, (*4, 13*) suggesting that it has a role in the regulation of extracellular matrix mineralization. Indeed, high FetA serum levels are found during fetal development when there is a high demand for mineral transport to the bone matrix. (*14, 15*) Based on the existence of fast transport pathways of calcium dyes from the blood to the bone matrix during embryonic bone development, FetA-based protein/mineral complexes have been proposed as mineral carriers during bone matrix formation. (*3, 16*)

While the formation of FetA/mineral complexes and their role in ectopic calcification has been studied quite extensively, the nanoscale dynamics of the assembly process and the exact role of FetA/mineral complexes in bone biomineralization remain to be elucidated. Here we use cryogenic and liquid phase electron microscopy in combination with dynamic light scattering to unravel the formation mechanism of CPP1 in fetal serum and subsequently investigate their potential for delivering mineral to the extracellular collagen matrix in osteogenic cell cultures. We find that CPP1 forms through a multistep assembly mechanism in which intraparticle dynamics rapidly decrease with CPP maturation and stable CPP1 carrying amorphous CaP (ACP) are formed within 24 min. Moreover, cell free *in vitro* experiments show that while freshly prepared FetA/CaP complexes containing mostly CPMs effectively mineralize collagen, mature solution containing CPP1 do not. We use *in vitro* osteogenic cell cultures to show that CPP1s are endocytosed by murine osteoblasts (MLO-A5), and that in the presence of these cells they act as an efficient mineral source, effectively substituting for the commonly used β-glycerophosphate. We conclude that although CPPs can act as effective transporters of mineral, mineral delivery to the collagen only takes place after cellular processing, most probably in the form of CPMs.

Primary CPPs Assemble via a Two-Phase Formation Process

FetA/CaP complexes were prepared from a complete cell culture medium containing minimal essential medium (αMEM) supplemented with 10% Fetal Calf Serum (FCS) upon incubation with 3.0 mM phosphate at 37°C. (*1, 3, 8*) This yields a biomimetic CPP formation medium with final concentration of 2.6 mg/mL FetA, 1.8 mM Ca^{2+} and 4.5 mM phosphate (Fig. S1A-B), similar to the standard concentrations used in osteogenic cell cultures. Dynamic light scattering (DLS) was used to dynamically monitor CPP formation while sampling the solution after the reaction for cryo-TEM analysis. DLS (Z-average) showed

a rapid increase of the particle hydrodynamic diameter between 18-26 min (Fig. 1A) after which it stabilizes at an average diameter of 105 nm. At this point also the increase in mean count rate leveled off (Fig. S1C, white/blue), implying the CPM-to-CPP transition was complete. Although the variation in CPP particle size decreased during the process, the final size distribution was still quite broad (60-420 nm intensity peak base, poly dispersity index 0.2-0.3, Fig S1D-E, blue), suggesting different levels of CPP development. Even after 24 h of incubation, cryo-TEM analysis showed a wide particle size distribution, with diameters ranging from 20-100 nm (Fig 1B). Cryo-TEM further revealed the CPPs were composed of many smaller sub-units (~2-5 nm), most likely CPMs (Fig 1B, inset).

Transient Complexes are Present in Developing CPP Formation Mixtures

To understand the dynamics of CPP formation by aggregation of CPMs and in particular the two stages of the assembly process we used liquid phase electron microscopy (LP-EM). LP-EM has recently been demonstrated to allow dynamic real-time visualization of CPP formation with nanoscale resolution, and without altering the kinetics of the assembly process. (*17*) The CPP formation medium (see Materials and Methods, Fig. 5) was encapsulated in graphene-liquid cells (GLC) using loop-assisted transfer (*17, 18*) and the grid was directly transferred to a TEM to study the early phases of primary CPP assembly (Fig. 1C-H). Starting from 13 minutes after phosphate addition, liquid pockets were imaged every 2 minutes at low electron dose (0.1 e^{-} $Å^{-2}$ per image) and at the end of the process, after 1h in the GLC, a high-contrast snapshot was recorded (10 e^{-} $Å^{-2}$ per image) to better visualize the borders of the liquid pocket (Fig. 1C, yellow line).

While the bulk DLS measurements showed a steady increase in particle size, LP-EM showed that particles with a small diameter (<50 nm) assembled and disassembled during the incubation period, which we refer to as transient CPPs (tCPPs, Fig. 1C-D, red arrow, Movie S1, left). Using thresholding and FIJI's analyze particles function, (*19*) the assembled structures were identified and color-coded based on their size (area, nm^2), to emphasize the growth and splitting of these small particles (Fig. 1E, Movie S1, right).

Mature Primary CPPs show Intraparticle Dynamics

In contrast to tCPPs, particles with diameters of ~100 nm did not grow further in size, nor did they show disassembly (Fig. 1F, blue arrows, Fig. S2A, Movie S2), suggesting they had matured to their maximum equilibrium size. Monitoring a small tCPP observed alongside mature CPPs still showed similar growth/disassembly dynamics (Fig. 1F,H, yellow arrows, Fig. S2B, Movie S3) as the previously discussed tCPPs (Figure 1D-E). This suggests that where feedstock (CPMs) was still present in the solution that allowed for growth of tCPPs, larger matured CPPs had been stabilized in size and shape by internal interactions.

Nevertheless, imaging of an aged CPP formation medium that had been incubated in a liquid pocket for 1 week showed the presence of CPP2 which were oval shaped and larger (~350 nm long axis) than the CPP1 and contained crystalline content (Figure S2D). This indicates that the CPPs in the liquid pocket showed similar development as previously observed in bulk samples in medium (*8*) and that the confined environment of the liquid pockets does not restrict the CPP dynamics that are responsible for maturation or growth. Indeed, structural dissimilarity index measure (DSSIM) analysis (*20*) showed a high dissimilarity within matured CPPs when sequential frames were compared (Fig. 1G). Imaging matured CPPs at higher temporal (but lower spatial) resolution (*17*) further revealed the internal dynamics with the composing CPMs moving within the confined space of the CPPs (Fig. S2C).

To further analyze the composition of the CPPs and CPMs, they were separated from the biomimetic CPP preparation medium after 24 h of incubation by spin filtration with 300 kDa and 3 kDa membranes, respectively. Subsequently protein, calcium and phosphate concentrations were determined by standard photometric and colorimetric analyses. This assay indicated that after 24h of incubation 60% of the Ca^{2+}, 18% of the phosphate (Ca:P ratio of 1.56, in line with the presence of ACP (*21, 22*)) and 65% of the protein (possibly including other proteins than FetA, e.g. albumin (*23*)) was bound in primary CPPs, with only 4% of the Ca^{2+} and ~11% of the phosphate and 35% of the protein fraction bound in the CPMs (Fig. S1B).

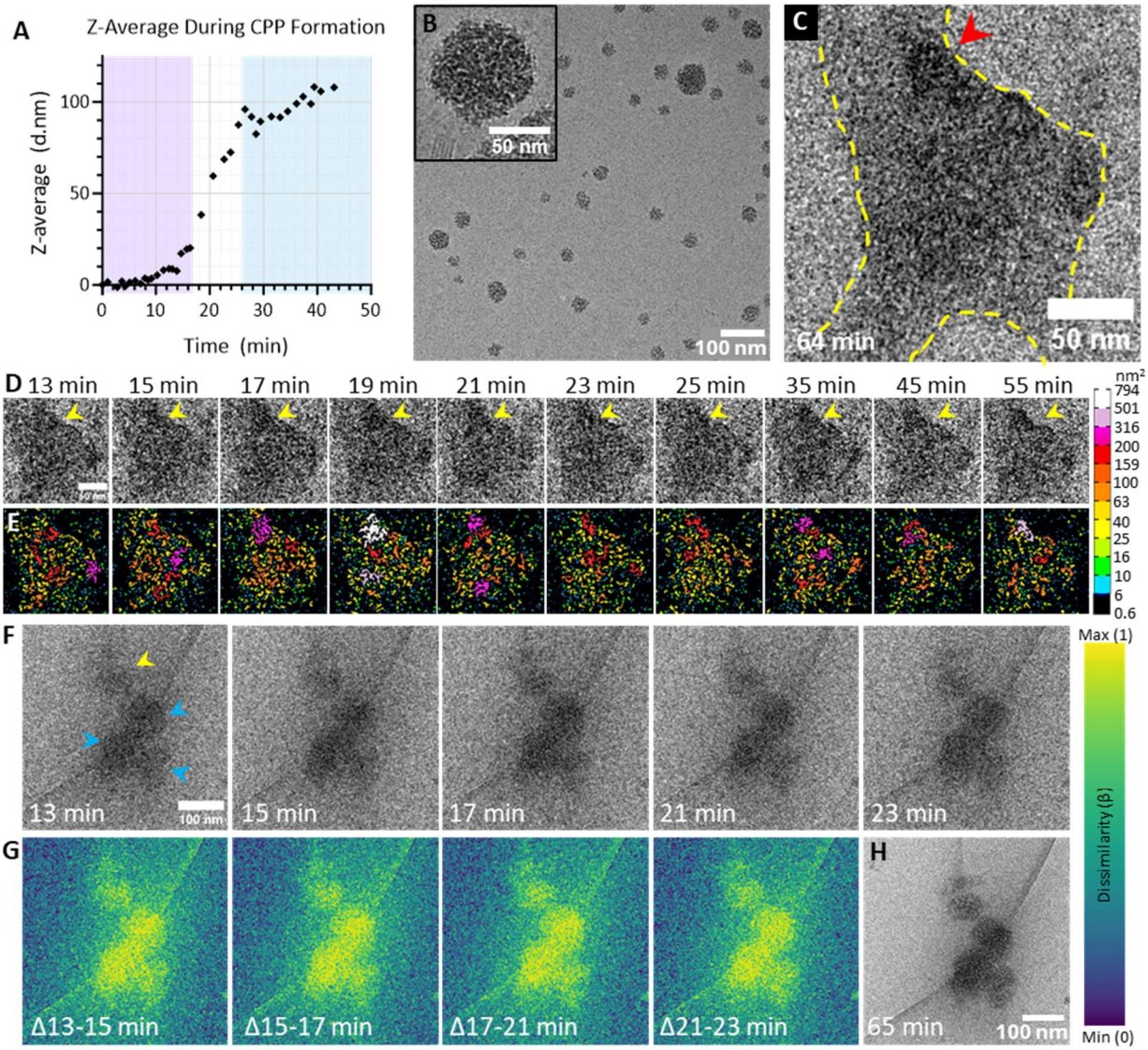

Fig. 1. Assembly of stable primary CPPs in cell culture medium is a two-phase process. (**A**) Time-resolved DLS shows a stable Z-average (close to 0 nm after background correction) in the first 16 minutes after addition of phosphate to complete cell culture medium (magenta). Next, the measured Z-average largely increases (white), after which a new size equilibrium (~105 nm) is reached around 25 minutes after the start of the reaction (blue). (**B**) CryoTEM shows the presence of spherical complexes with sizes ranging from 20 to 100 nm in complete cell culture medium supplemented with phosphate after 24h of incubation. The particles are composed of multiple smaller particles, as observed with high-resolution images (inset). (**C**) High-contrast snapshot (10 e^{-} $Å^{-2}$) of the GLC, recorded 64 min after the start of the reaction. Yellow dotted lines indicate the borders of the GLC. The largest CPP in the GLC is indicated with the red arrow. (**D**) Dynamic monitoring of GLC with LP-EM showed the formation of a small transient CPP (<50 nm, tCPP, yellow arrow) by assembly and disassembly of CPM clusters (0.1 e^{-} $Å^{-2}$ per image). The first image was recorded 13 min after addition of phosphate. Images were recorded every 2 minutes

(Movie S1, scalebar: 50 nm). (**E**) Color-based analysis of the tCPP (dis)assembly based on the measured size (area, nm^2) of particles identified with FIJI "analyze particles" after thresholding. Images match the grayscale images shown in (**D**). (**F**) Time-lapse LP-EM of a GLC containing three mature primary CPPs (>50 nm, blue arrows) and an area in which tCPP (dis)assembly is observed (<50 nm, yellow arrow, scalebar: 100 nm). (**G**) Structural dissimilarity index measure (DSSIM) analysis of sequential frames showed large changes within the particles. (**H**) High-contrast TEM image of the GLC after 65 min of incubation (10 $e^- Å^{-2}$) confirms the presence of 3 mature primary CPPs and a smaller tCPP.

FetA/Mineral Complexes are a Mineral Source for Osteoblasts

To investigate the capacity of FetA/mineral complexes to serve as a mineral source for bone biomineralization, we supplied them to an osteogenic cell culture of matrix-producing mouse osteoblasts (MLO-A5). (*24*) As a positive control, we used the commonly used phosphate source beta-glycerophosphate (βGP, 4mM) (*25, 26*) that is converted by alkaline phosphatase (ALP) expressed by the osteoblasts to generate phosphate. (*24*) After cells had proliferated until confluency (day 0) osteogenic medium was applied which consisted of 10% FCS in αMEM, supplemented with 100 µg/mL ascorbic acid to induce collagen production and the phosphate source (βGP or FetA/mineral complexes) to induce mineralization. After 14 days of culture in osteogenic medium, the progress of the mineralization process was visualized with fluorescence microscopy (Fig. 2).

In the βGP standard condition, fluorescent staining showed overlap of the collagen and mineral signals indicating mineralization of the matrix (Fig. 2A). In regions with a high mineral signal, the collagen signal had lower intensity due to lower accessibility for the collagen dye (CNA35-OG®488 (*27, 28*)) by the presence of the mineral (Fig. S3A). In a next step, FetA/mineral complexes were supplied to the osteogenic cell culture in the form of the biomimetic CPP formation medium that had been incubated for 24 h. Also in this experiment mineral deposition was observed in the collagen matrix by fluorescent imaging after 14 days of incubation (Fig. 2B). To exclude that the mineralization capacity of CPMs and possibly tCPPs present in the biomimetic CPP formation medium significantly contributed to the observed effects, we performed a parallel experiment with isolated preformed CPPs in a low FetA medium to balance for the excess FetA introduced through the added CPPs, while maintaining a total concentration of 1 mM phosphate (see Materials and Methods). Also in this case, a mineral pattern very similar to the βGP control experiments was observed after 14 days (Fig. 2C).

The potential role of FetA/mineral complexes in regulating matrix mineralization in bone biomineralization was further highlighted by the observation of early (day 7) and uncontrolled mineralization of the collagen matrix in βGP-supplemented low FetA cultures (Fig. S3B). Indeed, primary CPPs were also identified by cryoTEM analysis of medium taken from the βGP culture (day 7 of differentiation, Fig. S3C), implying that their formation is triggered by the ALP generated phosphate, potentially functioning as a mineral source also in these standard cultures.

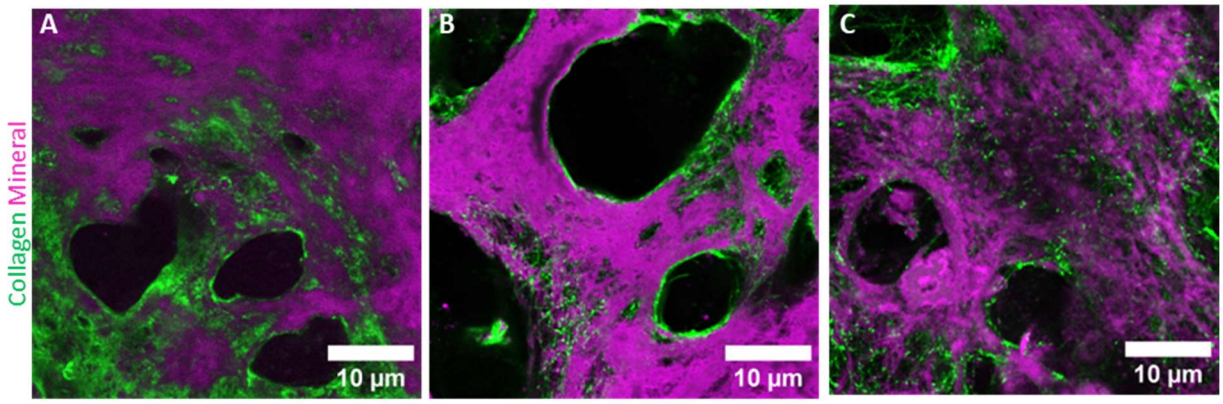

Fig. 2. FetA/mineral complexes can replace βGP as a mineral source in matrix-producing osteoblast cultures. Fluorescent images of a collagen matrix (CNA35-OG®488, green)) produced by osteoblasts and mineralized (Calcein Blue, magenta) in the presence of (**A**) βGP, (**B**) mixed FetA/mineral complexes containing CPPs and CPMs or (**C**) isolated CPPs. Collagen and mineral patterns follow a similar organization, indicating that the mineral signal is overlapping with the collagen signal. Single channel images are available in Fig. S3A.

Two Mineral Delivery Pathways Dependent on Maturity of the FetA/Mineral Complex

Direct Mineral Delivery by Immature Complexes

To investigate mechanistic details of the mineral delivery by the CPPs to the extracellular matrix of bone, we performed cryoTEM analysis of cell-free *in vitro* mineralization experiments, incubating bovine collagen type I on TEM grids with solutions containing FetA/mineral complexes. Surprisingly, the intrafirillar mineralization of the collagen fibrils was only observed with freshly prepared biomimetic CPP formation medium (Fig 3A), in a similar fashion as previously reported, (*29*) but not with biomimetic CPP formation medium that had been aged for 24 h (Fig. 3B) nor with isolated, more concentrated CPPs (Fig. 3C). In the latter cases the mineral remained retained in the stable CPPs, even after an incubation time of 21 (Fig. 3B) to 70 hours (Fig. 3C). This suggests that in these cell-free experiments collagen mineralization is facilitated by CPMs and/or tCPPs, rather than by matured, stable CPPs.

Mature CPPs Are Processed Intracellularly to Enable Mineral Deposition

Moreover, these results imply that there is a crucial role for the MLO-A5 cells in the conversion of the mineral in CPPs to bioavailable CaP that can mineralize the collagen. To shed light on this, the biomimetic CPP formation medium was spiked with fluorescently labeled FetA (CF®568-succinimidyl ester), while the calcium in the complexes was labeled with calcein green, allowing for dual-color fluorescence imaging of the CPPs (Figure 3D-E, Fig. S4). MLO-A5 osteoblasts were then incubated with fluorescently labeled FetA/mineral complexes, and the localization of the CPPs was studied with 3D fluorescence Airyscan® microscopy, by co-staining for cellular markers (actin, nuclei).

Dual-labeled particles were found overlapping with the cellular area of osteoblasts incubated with the FetA/mineral complex solution (Fig. 3D), while no signal was observed in either of the CPP channels in the negative control, to which no particles had been added (Fig. S4A). 3D reconstructions of high-resolution z-stacks indeed showed intracellular localization of the dual-colored CPPs, indicating their active internalization by the osteoblasts (Fig. 3E). Indeed, internalization decreased significantly in the presence of endocytosis inhibitors methyl-beta-cyclodextrin (*30, 31*) (MβCD, ~3.6x, p=0.0005) or Dynasore (*32*) (~4.6x, p=0.0004), while complete inhibition of internalization was achieved by cooling the cultures to 4°C (Fig. 3F-G, Fig. S4B-C).

The intracellular pathway of the CPPs could be further traced by imaging of living MLO-A5 cells incubated with fluorescently labeled CPPs in the presence of Lysotracker®, which stains acidic cellular components such as lysosomes. The observed colocalization of the FetA signal and the lysotracker signal (Pearson's coefficient: 0.7), (*33*) indicated that CPPs were indeed processed via the endo-lysosomal pathway after endocytosis (Fig. 3H). This indicates that cellular processing of FetA/mineral complexes, and specifically primary CPPs, is essential to facilitate mineral deposition induced by CPPs.

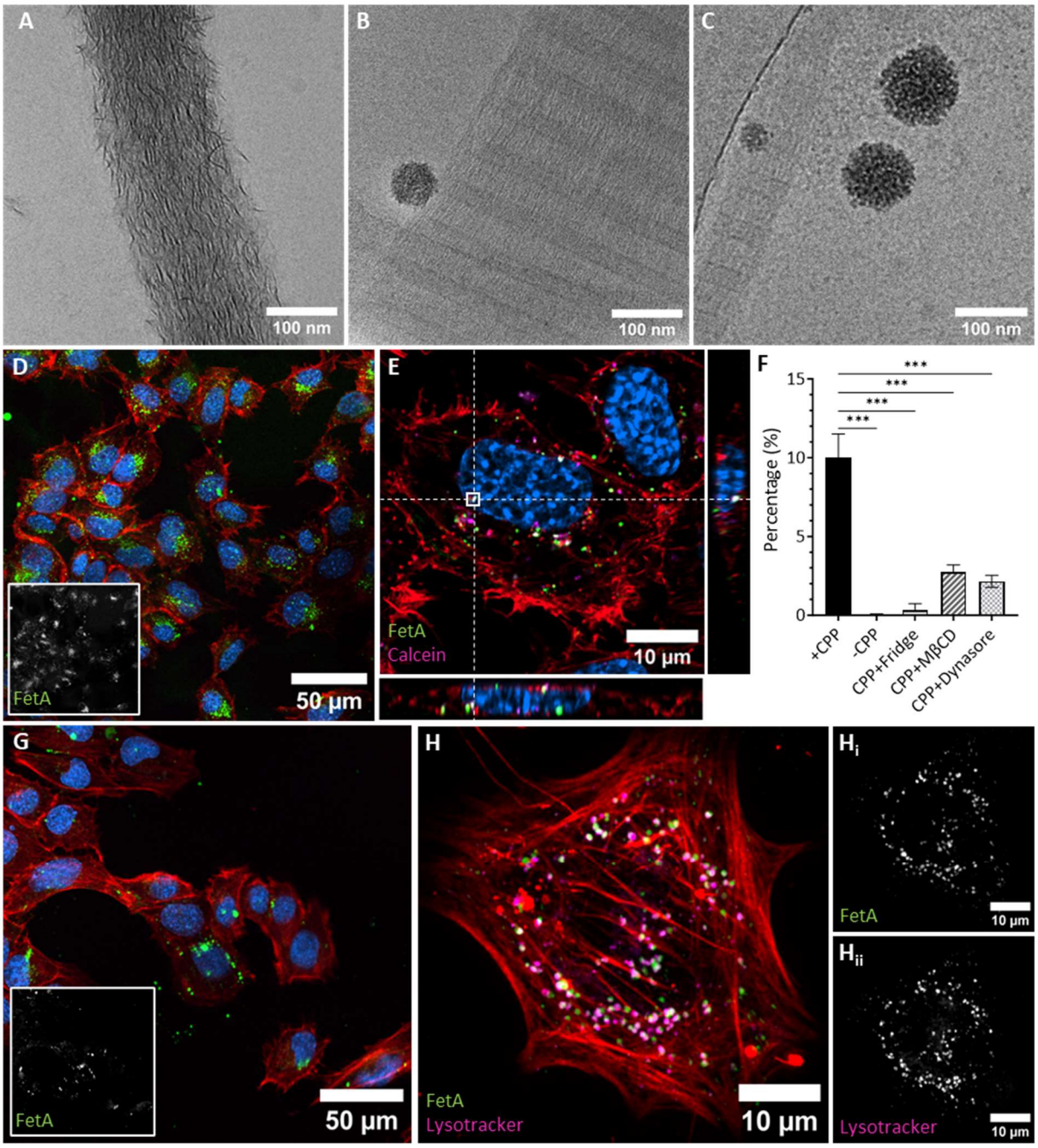

Fig. 3. Identification of two mineral delivery pathways by FetA/mineral complexes. (**A**) Cryo-TEM showed mineralized bovine collagen fibrils upon incubation (70 h) with freshly prepared biomimetic CPP formation medium. (**B**) Incubation (21 h) of bovine collagen fibrils with pre-formed mature FetA/mineral complexes (24 h old) showed no mineralization. (**C**) Incubation (70 h) of bovine collagen with concentrated, isolated mature CPPs (24 h old) did not result in collagen mineralization. (**D**) Fluorescent images of cells (actin: SiR-actin, red; nucleus: Hoechst 33342, blue) cultured in the presence of labeled FetA/mineral complexes (FetA-CF®568, green) showed FetA signal overlapping with cellular area. Inset: Isolated FetA channel. (**E**) Orthogonal views of 3D imaging show the presence of intracellular double labeled particles (FetA-CF®568, green; Calcein, magenta). (**F**) Quantification of intracellular FetA signal in the presence and absence of CPPs, as well as in the presence of CPPs under endocytosis inhibiting conditions. Significance calculated by ANOVA multiple comparison analysis in GraphPad Prism (*** $p<0.001$). (**G**) Representative images showing MLO-A5 osteoblasts (actin: SiR-actin, red; nuclei: Hoechst 33342, blue) incubated with labeled in the presence of endocytosis inhibitor methyl-β-cyclodextrin. Inset shows the isolated FetA channel. Representative images of the other conditions can be found in Fig. S4. (**H**) MLO-A5

osteoblasts (actin: SiR-actin, red) incubated with FetA-CF®568 labeled FetA/mineral complexes (green, **H**$_i$) and Lysotracker®-DND26 Green (magenta, **H**$_{ii}$) showing colocalization.

We have shown how elevated phosphate concentrations produce FetA/mineral complexes that act as precursors in the assembly of primary CPPs in a two-step process and showed the suitability of these complexes as a mineral source in osteogenic matrix mineralization via two mechanisms. CPP precursors (CPMs, tCPPs) can mineralize collagen in the absence of cells, while mature CPPs are only a viable source of mineral in the presence of osteoblasts that process the particles via endocytic pathways (Fig. 4). Similarly, high concentrations of FetA, (*14, 15*) calcium and phosphate in fetal blood (*34, 35*) likely increase the concentration of CPPs during fetal development. As the mineral transport capacity of CPPs is larger than that of CPMs - CPPs have been calculated to consist of around 100 of CPMs (*1*) - this would support the high demand for mineral during embryonic development more efficiently.

However, as CPPs in adults are cleared rapidly from the circulation by the liver, (*8*) and are mainly found in diseased individuals, the direct, low energy-demanding, delivery of mineral to the newly deposited bone matrix in adults by CPMs seems most plausible. It is thus conceivable that both pathways are involved in bone mineral transport during different stages of bone formation.

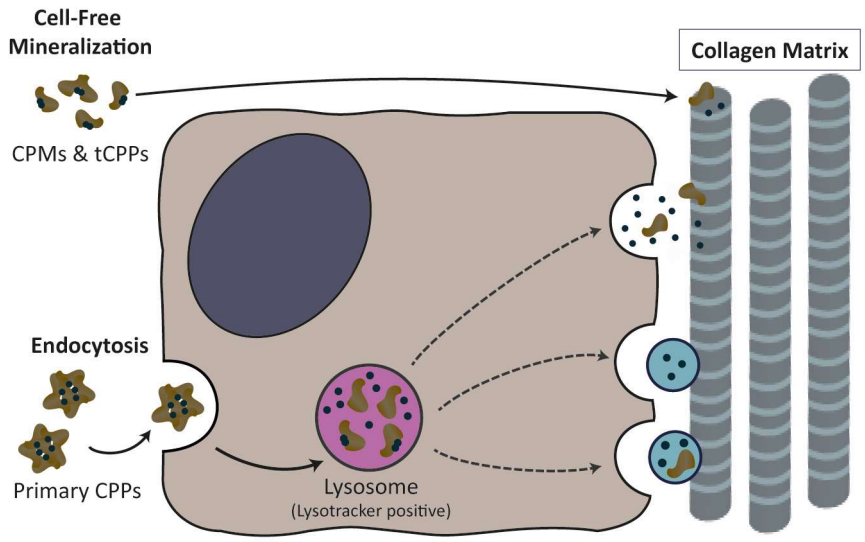

Fig. 4. Proposed pathways for CPM and CPP-based collagen mineralization. We showed that CPMs and tCPPs can directly deliver mineral to a collagen matrix, without the presence of cellular activity (direct transport), while mature primary CPPs need cellular processing to function as a source of mineral during osteogenic matrix mineralization (indirect transport). Our data indicate that CPPs are endocytosed and processed lysosomes (in pink). However, the secretion pathways of the mineral remain to be elucidated. Solid arrows indicate pathways shown in this study, dashed arrows show potential secretion pathways for which further confirmation is needed.

Materials and Methods

Fetuin-A fluorescent labeling

$NaHCO_3$ buffer (1 M, pH 8.27 at RT) was prepared. A small amount of CF®568 succinimidyl ester (Merck) was dissolved in DMSO (8 µL) and the dye concentration was determined based on absorbance (Nanodrop 2000c, ε=100.000, CF=0.08, Abs_{max}=562 nm). The initial concentration of the FetA monomer solution, purified on a Sephadex column (S. Gräber, RWTH Aachen), was determined based on the absorbance measured with the Nanodrop ($E_{1\%}$ of FetA: 0.45 mg ml^{-1} mm^{-1} at 280 nm; 23.8 mg/mL). The protein was diluted in PBS to reach a final concentration of 5 mg/mL, then $NaHCO_3$ buffer was added to the protein with final concentration of 0.1 M $NaHCO_3$ and the dye was added with a 1:10 molar ratio (protein:dye; final reaction mixture: 140.5 µL of 5 mg/mL FetA, 14.1 µL of $NaHCO_3$ buffer, 7 µL of

15.7 mM CF568). The protein-dye solution was vortexed briefly and incubated for 1h at room temperature in the dark on a shaker (300 rpm). Next, the solution was purified twice with an equilibrated Zeba Spin 7K MWCO Desalting column (ThermoFisher) via centrifugation (1000 g, 2 min) to remove the free dye. The concentration of labeled FetA (~5.3 mg/mL) and the degree of labeling (DOL) of FetA were determined to be around 3, based on measurements of the absorbance (562 nm (fluorescent dye), 280 nm (protein concentration)) and calculated using the following equations.

$$A\lambda_{protein-dye} = A\lambda_{max\,protein} - (A\lambda_{max\,dye}\ x\ CF))\ x\ dilution\ factor$$

$$\frac{A\lambda_{max\,protein-dy}}{[Protein]\ in\ mg/mL} = \frac{E1\%}{10\ mg/mL}$$

$$DOL\ in\ Moles\ Dye\ per\ Mole\ protein = \frac{A\lambda_{max\,dye}\ x\ dilution\ factor}{\varepsilon_{dye}\ x\ [Protein]\ in\ M}$$

Fetuin-A/mineral complex preparation

FetA mineral complexes were prepared according to two different protocols, dependent on the application. For direct application on cell cultures and collagen fibrils, FetA/mineral complexes were prepared in a solution of 10% FCS in αMEM (total volume 1 mL, Fig. 5). The solution was supplemented with NaH_2PO_4 (2.71 µL, 0.5 M stock) and Na_2HPO_4 (4.28 µL, 0.5 M stock) and incubated for 24 h at 37°C.

For purification and dilution in cell culture medium, complexes were prepared by mixing pre-warmed FCS (400 µL) with NaCl (100 µL, 140 mM), phosphate buffer (250 µL, 40 mM NaCl, 19.44 mM Na_2HPO_4, 4.56 mM $NaH_2PO_4 \cdot 1H_2O$, pH 7.4) and calcium stock (250 µL, 140 mM NaCl, 40 mM $CaCl_2 \cdot 2H_2O$, 100 mM HEPES). The solution was incubated at 37°C (10 min). Particles were pelleted (20000 g, 20 min, 4°C) and pellets were resuspended in αMEM. Then, CPPs were isolated and further concentrated on 300000 MWCO Vivaspin 2 filters (10 min, 3000 g, RT).

For fluorescent labeling of the FetA/mineral complexes, labeled FetA was added in a molar ratio of 1:100 before the incubation was started. Additionally, for dual labeling, Calcein Green (1 µg/mL in 100 mM KOH) was added during the last hour of incubation.

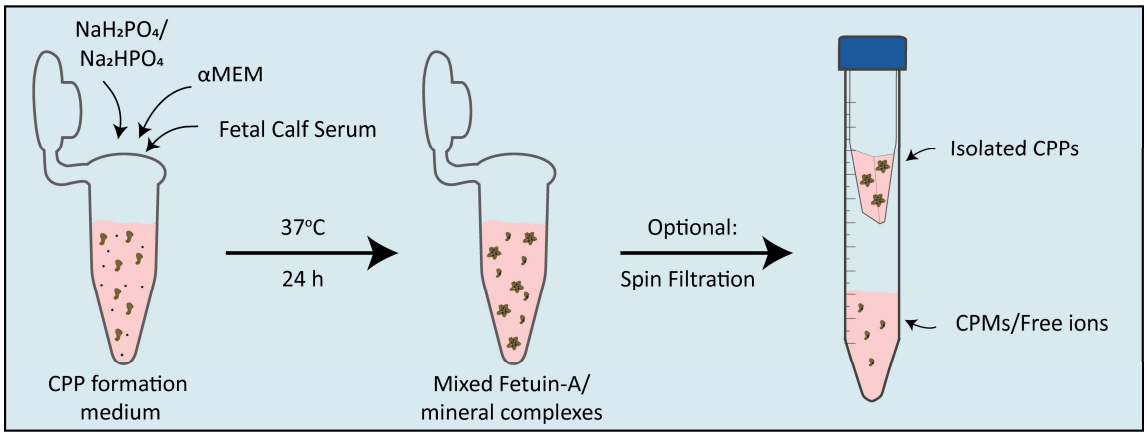

Fig. 5. Preparation process of FetA/mineral complexes in osteoblast medium. CPP formation medium, containing αMEM supplemented with FCS and phosphate was incubated at 37°C for 24 h to stimulate formation of CPPs. If indicated, CPPs were separated from CPMs and free ions by spin filtration.

Liquid Phase Electron Microscopy

Copper chips coated with graphene by CVD were placed inside a Naiad-1 (VitroTEM) and the copper was etched away with 0.2 M ammonium persulfate. Next, the free-floating graphene was washed with Milli-Q. A small volume (40 µL) of CPP formation medium was prepared in cell culture medium as described

above (αMEM/10% FCS/NaH_2PO_4 (0.11 µL, 0.5 M stock)/Na_2HPO_4 (0.17 µL, 0.5 M stock)). 5 µL of the mixed solution was applied on a gold 200 mesh ultrathin carbon film finder TEM grid (CF200F1-AU-UL, Electron Microscopy Sciences) and samples were encapsulated in 96% humidity with graphene by automated loop-transfer using a Naiad-1 system (VitroTEM).

After encapsulation, the grid was transferred to an Elsa cryo-transfer holder (Gatan) and placed in a TALOS F200c G2 TEM (Thermo Fisher) equipped with a Falcon 4i direct electron detector (Thermo Fisher) operated at 200 kV. Images were acquired every 2 minutes at 37 °C, using low-dose imaging (0.1 $e^- Å^{-2}$) until the samples had been incubated 1 h. After 1 h, a high-contrast snapshot was recorded (10 $e^- Å^{-2}$).

Cell culture

MLO-A5 osteoblasts were obtained from Kerafast (*24*) and cultured according to the suppliers instructions. In short, cells were proliferated in αMEM (22571) supplemented with 5% FCS and 5% BCS (Hyclone, SH30073) in a humidified incubator (37°C, 5% CO_2) and split 1:20 twice a week after detaching with Trypsin/EDTA (0.05%/0.53 mM).

For mineralization experiments, MLO-A5 cells were seeded on HCl (1 M) washed and ethanol (70%) sterilized coverslips (#1.5). The cells were proliferated until confluent before osteogenic medium was applied. For classical mineralization, the medium consisted of 10% FCS in αMEM, supplemented with 100 µg/mL ascorbic acid (AA), 100 U/mL-100 µg/mL Penicillin/Streptomycin (PenStrep), and 4 mM of beta-glycerophospate (βGP). For mineralization in the presence of mixed FetA/mineral complexes, the FetA/mineral complex preparation was removed from the water bath after 24h of incubation and supplemented with AA (100 µg/mL) and PenStrep (100 U/mL-100 µg/mL).

For mineralization in the presence of isolated CPPs, the medium consisted of 10% BCS in αMEM, supplemented with 100 µg/mL AA, PenStrep (100 U/mL-100 µg/mL) and isolated CPPs with a concentration of 1 mM phosphate, as determined based on the calcium concentration of the particles. BCS instead of FCS was used to overcome overloading of the culture with FetA, that is also naturally present in the complete culture medium because of FCS supplementation. BCS contained approximately 8.5x less FetA ([$FetA_{BCS}$] = 3.1 mg/mL; [$FetA_{FCS}$] = 26.4 mg/mL) as determined by western blotting (Fig. S1A).

Collagen production and mineralization were monitored at fixed time points (d7/d14) by fixing the cells in paraformaldehyde (PFA, 4%, RT, 15 min) and staining with CNA35-OG®488 (*27, 28*) (1 µM), Calcein Blue (0.1 mg/mL) and Phalloidin-Alexa Fluor® 568 in PBS (1h, RT). After staining, the samples were washed twice in PBS and mounted in Vectashield.

Fluorescence images were recorded on an LSM900 upright with Airyscan® 2 detector (Carl Zeiss Microscopy GmbH, Germany). Overviews were recorded using a 20x (NA 0.8) objective in SR-4Y mode. High resolution z-stacks were recorded using a 63x oil immersion objective (NA 1.4), using SR Airyscan mode.

Calcium assay

Concentrations of isolated CPPs were determined using an O-cresolphthalein based calcium assay (Randox). Calcium was dissolved from the CPPs by mixing two volumes of CPPs sequentially with one volume of HCl (0.6 M) and one volume of 40 mM NH_4Cl/5% NH_4OH. Samples were diluted 125x and 250x in dH_2O and were mixed with the prepared kit reagents. The kit reagents (component A and B) were mixed in equal volumes before use and 250 µL was added to the samples and $CaCl_2$ standards (20 µL).

After incubation (15 min, RT), the absorption was measured with a platereader (570 nm, Biorad Benchmark Plus). The concentration of calcium in the samples was calculated and the phosphate concentration was determined based on the Ca:P ratio of amorphous calcium phosphate (1.6 (*21, 22*)).

Endocytosis inhibition assay

MLO-A5 cells (1000 cells per cm^2) were seeded on coverslips (#1.5) and cultured for 3 days. FetA/mineral complexes were prepared as described above, in the presence of fluorescently tagged FetA and Calcein Green. The cells were pre-incubated under endocytosis inhibiting conditions (fridge/methyl-beta-cyclodextrin (2.5 mM)/Dynasore (40 µM)) for 30 min before the proliferation medium was exchanged for FetA/mineral complex medium, supplemented with AA and PenStrep. The cells were incubated with the FetA/mineral complexes for 4 h under variable conditions: standard conditions, in the fridge, and in the presence of methyl-beta-cyclodextrin (2.5 mM) or Dynasore (40 µM). After incubation, the cells were washed with PBS (3x) and fixed in 4% PFA (15 min, RT). After fixation, cells were stained with Hoechst 33342 (1 µg/mL) and silicon-rhodamine F-Actin (SiR-Actin, Spirochrome, 1 µM) for 1 h. Next, the coverslips were washed twice in PBS and mounted with Vectashield on glass slides.

Fluorescence images were recorded on a LSM900 upright with Airyscan 2 detector. Overviews were recorded using a 20x Plan-Apochromat objective (NA 0.8) in SR-4Y mode. High resolution z-stacks were recorded using a 63x Plan-Apochromat oil immersion objective (NA 1.4), using SR Airyscan mode.

For quantification of the intracellular FetA signal, 20x images were processed in FIJI.(*36*) Based on the actin signal, a mask for cellular localization was made using automated thresholding (Li (*37*)) and holes in the cells were filled to cover the full cellular surface. The cellular surface area was calculated by measuring the area of the actin mask using the Analyze Particles function (size: 5 or 20-infinity (5 positive and negative control, 20 for experimental conditions)). Next, the particles overlapping with the cellular area were selected using the AND function on the actin mask and the FetA channel. The FetA channel was automatically tresholded (Yen (*38*)) to prepare a mask and particle analysis (size: 0-infinity, circularity: 0-1) was performed to measure the sum of the surface area calculated with the ROI manager. The calculated surface values were used to determine the percentage of the cellular area that overlapped with the FetA signal. Statistical testing was performed in GraphPad Prism version 10.1.2 (GraphPad Software, Boston, Massachusetts USA, www.graphpad.com) by performing a one-way ANOVA followed by Dunnett's multiple comparisons test.

Sub-cellular CPP localization

MLO-A5 cells were seeded and cultured as described for the endocytosis inhibition assay. After 3 days in proliferation medium, the cells were incubated with FetA labeled FetA/mineral complexes for 4 to 6 h and stained live with Hoechst 33342 (1 µg/mL) and SiR-actin (1 µM) in the presence of Verapamil (10 µM) for 1 h. Shortly before imaging, the FetA/mineral complex medium was replaced by imaging medium without FetA/mineral complexes, consisting of 10% FCS in αMEM, supplemented with 100 µg/mL AA, PenStrep (100 U/mL-100 µg/mL), Verapamil and Lysotracker® Green DND-26 (0.5 µM). The cells were imaged live using an LSM900 upright with Airyscan 2 detector in SR-4Y mode, using a 63x water dipping objective (W Plan-Apochromat, NA 1.0).

Cell-free mineralization and cryoTEM

For cell-free mineralization experiments, 5 µL of bovine tendon collagen (0.8 mg/mL collagen in 0.5 mM acetic acid) was loaded on a gold 200 mesh plasma treated Quantifoil R2/2 grid. After 10 min, the excess liquid was blotted away. The collagen-loaded grid was incubated for 21 h or 70 h on a droplet of FetA/mineral complex solution (either directly after preparing (21 h), or after concentrating CPPs 6.25x on a Vivaspin 300000 MWCO filter (70 h)) in a humidity chamber at 37°C. Next, the grids were

vitrified using a VitroBot Mark IV and images were acquired using a JEOL JEM 2100 (Jeol Ltd., Tokyo, Japan) equipped with a Gatan 890 Ultrascan (Pleasanton, CA, USA) and LaB6 filament operated at 200 kV using low dose software (Serial EM).

To study the mineralization capacity of the FetA/mineral complex solution before CPP formation, collagen-loaded TEM grids were incubated in a FetA/mineral complex preparation solution, before 24h incubation in the water bath. Grids were incubated for 70h in 100% humidity before vitrification and imaging.

To analyze CPP preparations and the presence of CPPs in βGP-supplemented cell culture medium, a sample of medium that had been incubated on a differentiating culture was taken at day 7 of differentiation before medium exchange and vitrified using a VitroBot Mark IV as described above, before imaging at the JEOL JEM 2100.

DLS

To confirm particle size, DLS measurements were performed on the Zetasizer Pro (timelapse). The FetA/mineral complex solution was measured directly after production of the particles to determine particle size. For timelapse measurements, 10% FCS in αMEM was measured at 37°C before the additional phosphate was added (for background correction). After phosphate addition, measurements were taken approximately every 90 seconds during the first 40 minutes, while incubating the solution in the Zetasizer at 37°C. Single timepoints of later stages of particle formation were recorded after 1 h, 2 h, 4 h, 21 h, 48 h and 77 h. Plots were prepared in GraphPad Prism version 10.1.2.

Blood Test

Concentrations of calcium, phosphate and protein in the fractions of the FetA/mineral complex solutions were determined based on standardized tests from the hospital (Diagnostics Laboratory Radboudumc). FetA/mineral complexes were prepared as above and isolated using spin filtering with 300000 MWCO Vivaspin filters (4000 g, 10-15 min, CPP in retentate, CPM and ions in flowthrough) and 3000 MWCO Vivaspin filters (4000 g, 10-15 min, CPM in retentate, ions in flowthrough). Calcium measurements were based on a photometric test with 5-nitro-5'-methyl-BAPTA and EDTA. Phosphate concentration was determined based on a photometric test with ammonium molybdate. Protein concentration was determined using a colorimetric assay in which a biuret complex with Cu^{2+} was formed in an alkaline solution. Photometric and colorimetric measurements were performed on a ROCHE Cobase 8000, module C702.

Western Blot

Western blots were used to analyze the concentration of FetA in FCS and BCS. Three known concentrations of FetA were loaded next to three dilutions of FCS and BCS on a stain-free TGX gradient gel (4-15%, Biorad). After running (200V, 30 min), total protein loading was visualized using a GelDoc and the proteins were blotted to an activated PVDF membrane using a Trans-Blot Turboblotter (Biorad). After blotting, the blot was incubated overnight (4°C) in rabbit-anti-FetA (developed at RWTH Aachen) in PBS/0.1% Tween-20 (PBST). Next, the blot was washed 3x in PBST and incubated with a goat-anti-rabbit IRDye-800 secondary antibody, before imaging on an Odyssey Clx (LI-COR). Protein concentrations were quantified based on the net pixel intensity of the bands in FIJI.(*36*) The band areas per lane were selected using a consistent ROI frame size based on the largest band area. Next, background areas above and below each band were selected using a consistent ROI frame size. All areas were measured for mean gray values and the net pixel intensity value of the band was derived by subtracting the average of the two background gray values from the band gray value.

Image Processing

LP-EM images were processed in FIJI (v1.53t), (*36*) by applying a gaussian blur filter (σ=1 (pixel)). Next, the images were imported in Dragonfly 3D World 2024.1 (Comet Technologies Canada Inc., Montreal, Canada; software available at https://www.theobjects.com/dragonfly) and slice registration was performed to align the images. First, manual adjustments were made to remove large jumps. Then automated registration was performed using "optical flow" and allowing only translation. Lastly, manual adjustments were made to optimize the alignment. After aligning, liquid pockets were cropped out of the image and FIJI was used to apply thresholding for particle analysis with default settings (size: 0-infinity, circularity: 0.00-1.00) to determine the size of the particles. Next, the ROI color coder from the Broadly Applicable Routines (BAR) plugin in FIJI was used to color the particles based on their size (logarithmic scale bar). Additionally, the cropped liquid pockets were analyzed by DSSIM analysis in FIJI (standard deviation 1.5, size 11, per-frame contrast, α=0 β=1 γ=0). (*20*)

Fluorescence images were processed in FIJI. For visualization purposes, window/level values were adjusted. In cases of comparison between multiple conditions, these settings were adapted per experiment for all conditions. Z-stack maximum intensity projections were prepared for visualization and stacks were resliced (left and top) to prepare orthogonal views.

Acknowledgements

The authors would like to thank Steffen Gräber for the purification of the Fetuin-A used for fluorescent labeling. The authors also thank Thomas Kock and Gregory Schneider from Leiden University for supplying the graphene coated chips used in the LP-EM experiments. JS, LS, ST, AS, MM, and NS were supported by a European Reseach Council (ERC) Advanced Investigator grant (H2020-ERC-2017-ADvV-788982-COLMIN). AA was supported by a VENI grant from the Netherlands Scientific Organization NWO (VI.Veni.192.094). EMS was supported by the Research Program Ramón y Cajal (RYC2023-045512-I) funded by MCIN/AEI/10.13039/501100011033 and FSE+, and the project PID2022-141993NA-I00 funded by MICIU/AEI/10.13039/501100011033 and ERDF/UE. WJ-D received funding from the Deutsche Forschungsgemeinschaft (DFG, German Research Foundation, Project-ID 322900939 and 403041552).

References

1. A. Heiss *et al.*, Structural basis of calcification inhibition by alpha 2-HS glycoprotein/fetuin-A. Formation of colloidal calciprotein particles. *J. Biol. Chem.* **278**, 13333-13341 (2003). 10.1074/jbc.M210868200.
2. A. Heiss, V. Pipich, W. Jahnen-Dechent, D. Schwahn, Fetuin-A is a mineral carrier protein: small angle neutron scattering provides new insight on Fetuin-A controlled calcification inhibition. *Biophys. J.* **99**, 3986-3995 (2010). 10.1016/j.bpj.2010.10.030.
3. W. Jahnen-Dechent *et al.*, Mud in the blood: the role of protein-mineral complexes and extracellular vesicles in biomineralisation and calcification. *J. Struct. Biol.* **212**, 107577 (2020). 10.1016/j.jsb.2020.107577.
4. W. Jahnen-Dechent, A. Heiss, C. Schafer, M. Ketteler, Fetuin-A regulation of calcified matrix metabolism. *Circ. Res.* **108**, 1494-1509 (2011). 10.1161/CIRCRESAHA.110.234260.
5. E. R. Smith, T. D. Hewitson, W. Jahnen-Dechent, Calciprotein particles: mineral behaving badly? *Curr. Opin. Nephrol. Hypertens.* **29**, 378-386 (2020). 10.1097/MNH.0000000000000609.
6. W. Jahnen-Dechent, E. R. Smith, Nature's remedy to phosphate woes: calciprotein particles regulate systemic mineral metabolism. *Kidney International* **97**, 648-651 (2020). 10.1016/j.kint.2019.12.018.
7. S. Köppert *et al.*, Live Imaging of Calciprotein Particle Clearance and Receptor Mediated Uptake: Role of Calciprotein Monomers. *Front. Cell. Dev. Biol.* **9**, 633925 (2021). 10.3389/fcell.2021.633925.
8. S. Köppert *et al.*, Cellular Clearance and Biological Activity of Calciprotein Particles Depend on Their Maturation State and Crystallinity. *Front. Immunol.* **9**, 1991 (2018). 10.3389/fimmu.2018.01991.
9. E. R. Smith, T. D. Hewitson, E. Hanssen, S. G. Holt, Biochemical transformation of calciprotein particles in uraemia. *Bone* **110**, 355-367 (2018). 10.1016/j.bone.2018.02.023.

10. E. R. Smith *et al.*, Phosphorylated fetuin-A-containing calciprotein particles are associated with aortic stiffness and a procalcific milieu in patients with pre-dialysis CKD. *Nephrology Dialysis Transplantation* **27**, 1957-1966 (2012). 10.1093/ndt/gfr609.
11. S. Rudloff, W. Jahnen-Dechent, U. Huynh-Do, Tissue chaperoning-the expanded functions of fetuin-A beyond inhibition of systemic calcification. *Pflugers Arch* **474**, 949-962 (2022). 10.1007/s00424-022-02688-6.
12. P. Aghagolzadeh *et al.*, Calcification of vascular smooth muscle cells is induced by secondary calciprotein particles and enhanced by tumor necrosis factor-&#x3b1. *Atherosclerosis* **251**, 404-414 (2016). 10.1016/j.atherosclerosis.2016.05.044.
13. D. Toroian, P. A. Price, The essential role of fetuin in the serum-induced calcification of collagen. *Calcif. Tissue Int.* **82**, 116-126 (2008). 10.1007/s00223-007-9085-2.
14. M. Häusler, C. Schäfer, C. Osterwinter, W. Jahnen-Dechent, The Physiologic Development of Fetuin-A Serum Concentrations in Children. *Pediatric Research* **66**, 660-664 (2009). 10.1203/PDR.0b013e3181bc3f60.
15. W. Jahnen-Dechent, A. Pasch, Solving the insoluble: calciprotein particles mediate bulk mineral transport. *Kidney International* **103**, 663-665 (2023). https://doi.org/10.1016/j.kint.2023.01.011.
16. A. Akiva *et al.*, Intercellular pathways from the vasculature to the forming bone in the zebrafish larval caudal fin: Possible role in bone formation. *J. Struct. Biol.* **206**, 139-148 (2019). 10.1016/j.jsb.2019.02.011.
17. L. Rutten *et al.*, A Cryo-to-Liquid Phase Correlative Light Electron Microscopy Workflow for the Visualization of Biological Processes in Graphene Liquid Cells. *Adv. Funct. Mater.*, (2024). 10.1002/adfm.202416938.
18. P. M. G. van Deursen *et al.*, Graphene Liquid Cells Assembled through Loop-Assisted Transfer Method and Located with Correlated Light-Electron Microscopy. *Adv. Funct. Mater.* **30**, 1904468 (2020). 10.1002/adfm.201904468.
19. W. S. Rasband. (U. S. National Institutes of Health, Bethesda, Maryland, USA, 1997-2018), available at https://imagej.net/ij/.
20. J. T. Mulvey *et al.*, Correlating electrochemical stimulus to structural change in liquid electron microscopy videos using the structural dissimilarity metric. *Ultramicroscopy* **257**, 113894 (2024). 10.1016/j.ultramic.2023.113894.
21. J. Zhao, Y. Liu, W.-b. Sun, X. Yang, First detection, characterization, and application of amorphous calcium phosphate in dentistry. *J. Dent. Sci.* **7**, 316-323 (2012). 10.1016/j.jds.2012.09.001.
22. S. V. Dorozhkin, Synthetic amorphous calcium phosphates (ACPs): preparation, structure, properties, and biomedical applications. *Biomater. Sci.* **9**, 7748-7798 (2021). 10.1039/D1BM01239H.
23. D. Y. Lee *et al.*, Review of the Current Research on Fetal Bovine Serum and the Development of Cultured Meat. *Food Science of Animal Resources* **42**, 775-799 (2022). 10.5851/kosfa.2022.e46.
24. Y. Kato *et al.*, Establishment of an Osteoid Preosteocyte-like Cell MLO-A5 That Spontaneously Mineralizes in Culture. *J. Bone Miner. Res.* **16**, (2001). 10.1359/jbmr.2001.16.9.1622.
25. H. C. Tenenbaum, Role of Organic Phosphate in Mineralization of Bone in vitro. *J. Dent. Res.* **60**, 1586-1589 (1981). 10.1177/00220345810600030801.
26. J. M. Schaart *et al.*, Cell-induced collagen alignment in a 3D in vitro culture during extracellular matrix production. *J. Struct. Biol.* **216**, 108096 (2024). 10.1016/j.jsb.2024.108096.
27. K. N. Krahn, C. V. Bouten, S. van Tuijl, M. A. van Zandvoort, M. Merkx, Fluorescently labeled collagen binding proteins allow specific visualization of collagen in tissues and live cell culture. *Anal. Biochem.* **350**, 177-185 (2006). 10.1016/j.ab.2006.01.013.
28. R. A. Boerboom *et al.*, High resolution imaging of collagen organisation and synthesis using a versatile collagen specific probe. *J. Struct. Biol.* **159**, 392-399 (2007). 10.1016/j.jsb.2007.04.008.
29. F. Nudelman *et al.*, The role of collagen in bone apatite formation in the presence of hydroxyapatite nucleation inhibitors. *Nat. Mater.* **9**, 1004-1009 (2010). 10.1038/nmat2875.
30. J. J. Rennick, A. P. R. Johnston, R. G. Parton, Key principles and methods for studying the endocytosis of biological and nanoparticle therapeutics. *Nat. Nanotechnol.* **16**, 266-276 (2021). 10.1038/s41565-021-00858-8.
31. D. Vercauteren *et al.*, The Use of Inhibitors to Study Endocytic Pathways of Gene Carriers: Optimization and Pitfalls. *Mol. Ther.* **18**, 561-569 (2010). 10.1038/mt.2009.281.
32. E. Macia *et al.*, Dynasore, a Cell-Permeable Inhibitor of Dynamin. *Dev. Cell* **10**, 839-850 (2006). 10.1016/j.devcel.2006.04.002.

33. S. Bolte, F. P. Cordelières, A guided tour into subcellular colocalization analysis in light microscopy. *J Microsc*, (2006).
34. C. S. Kovacs, Bone metabolism in the fetus and neonate. *Pediatr. Nephrol.* **29**, 793-803 (2014). 10.1007/s00467-013-2461-4.
35. C. S. Kovacs, Calcium, phosphorus, and bone metabolism in the fetus and newborn. *Early Hum. Dev.* **91**, 623-628 (2015). 10.1016/j.earlhumdev.2015.08.007.
36. J. Schindelin *et al.*, Fiji: an open-source platform for biological-image analysis. *Nat. Methods* **9**, 676-682 (2012). 10.1038/nmeth.2019.
37. C. H. Li, P. K. S. Tam, An iterative algorithm for minimum cross entropy thresholding. *Pattern Recog. Lett.* **19**, 771-776 (1998). 10.1016/S0167-8655(98)00057-9.
38. J.-C. Yen, F.-J. Chang, S. Chang, A new criterion for automatic multilevel thresholding. *IEEE Transactions on Image Processing* **4**, 370-378 (1995). 10.1109/83.366472.